MATERIALS SCIENCE

Harmonic-induced plasmonic resonant energy transfer between metal and semiconductor nanoparticles

Yueming Yan[1], Nathan J. Spear[2], Adam J. Cummings[1], Karina Khusainova[1], Janet E. Macdonald[3], Richard F. Haglund[1]*

Heterostructures combining two or more metal and/or semiconductor nanoparticles exhibit enhanced upconversion arising from localized nanoparticle resonances. However, plasmon-exciton coupling in semiconductor-metal nanostructures exhibits nanosecond relaxation times, and multi-plasmon metallic heterostructures are not broadly tunable. Here, we develop a biplasmonic heterostructure in which CuS and Au nanoparticle layers, separated by an alumina spacer of variable thickness, exhibit enhanced second- and third-harmonic generation due to dipole-dipole coupling between Au and CuS plasmons, as seen in the characteristic inverse sixth-power dependence of their separation in the measured harmonic enhancement and confirmed by numerical simulations of near-field CuS-Au nanoparticle coupling. Transient-absorption spectroscopy shows faster relaxation in Au/CuS (690 femtoseconds) compared to CuS heterostructures (929 femtoseconds). Moreover, nonlinear absorption measurements provide evidence for harmonic-induced plasmonic resonant energy transfer between the narrow Au and broad, tunable CuS plasmon resonances. This prototype for ultrafast upconversion showcases a strategy for high-efficiency, tunable plasmonic nonlinear devices with promising applications in photocatalysis, parametric down-conversion, and biomedical imaging.

INTRODUCTION

Ultrafast nonlinear optical devices that can upconvert photon frequencies have applications in fields ranging from optical communications to medical diagnostics (*1*–*3*). Metal-nanoparticle (NP) systems have long been known to exhibit strongly enhanced upconversion effects, such as harmonic generation (*4*–*6*) and multiphoton photoluminescence (MPPL) (*7*–*10*) mediated by large local electric field generated by localized surface plasmon resonances (LSPRs), collective oscillations of surface charge carriers excited at the resonant plasmon frequency. To further increase nonlinear performance, multiplasmonic structures featuring harmonically coupled plasmonic resonances—one at the excitation wavelength and the other at a harmonic frequency of that wavelength—have also attracted substantial interest. In these structures, multiple plasmon resonances can be excited by plasmon-plasmon interactions driven at a fundamental resonance frequency, leading to substantial electric-field enhancements at both fundamental and harmonic frequencies. Most of the relevant studies on multiplasmonic structures are based on metallic NPs prepared by lithographic techniques, in which either multipole (*11*) or multimodal (*12*) plasmon resonances are excited in a single metallic crystal or by incorporating structures with two different metallic particles in which the plasmon resonance in both metallic components satisfies the harmonic condition (*13*). However, in metal dual-plasmon nanostructures, major challenges include the high cost of lithographic nanofabrication and the inherently narrow bandwidth of metallic NP LSPRs, which severely limits the tuning range of absorption and emission.

The broad LSPRs of semiconductor NPs, on the other hand, enable tuning from the visible to the mid-infrared by varying NP size, geometry, and doping level (*14*, *15*). Hence, this emerging class of plasmonic hetero-nanocomposites, integrating metal and semiconductor NPs synthesized by solvothermal processes, exhibits not only extraordinary tunability but also compatibility with large-area preparation techniques, such as dip coating or painting. Previous studies have shown that metal-semiconductor heterostructures feature strongly enhanced light absorption and are attractive for photothermal therapy and solar energy applications (*16*–*19*). An extreme example of high absorption is provided by Janus metal-semiconductor NPs suspended in liquid, which exhibit ultrafast enhanced light absorption due to plasmon-induced hot-electron injection (*20*, *21*), but not light emission. However, the liquid environment limits the potential for incorporating these nanostructures into nonlinear frequency conversion devices. Many studies in photothermal therapy and solar energy conversion have reported enhanced upconversion in coupled metal-semiconductor NP systems by plasmon-exciton coupling (*22*–*24*), in which upconverted emission from recombination of excitons in the semiconductor is boosted by the local electric field from proximate metal plasmons. However, the timescales of exciton relaxation are substantially slower than those observed in metallic plasmon-plasmon coupling.

Unlike the numerous studies on enhanced light absorption in metal-semiconductor plasmonic nanocomposites, we focus here on ultrafast light emission following the excitation of semiconductor and metal LSPRs. In Au/CuS dual-plasmon NP heterostructure films, spectral overlap between the second harmonic of the CuS LSPRs (1050 nm) and the fundamental mode of the Au LSPRs (525 nm) allows these dipolar plasmon resonances to be simultaneously excited by two-photon absorption of intense near-infrared (NIR) laser pulses (1050 nm), coupling and transferring the second harmonic energy to each other via surface dipole-dipole interactions that depend on the inverse sixth power of their separation (*25*). This plasmonic coupling enables bidirectional resonant energy transfer, leading to enhanced second-harmonic generation (SHG) and third-harmonic generation (THG). We call this process harmonic-induced plasmonic resonant energy transfer (HIPRET) between the plasmonic semiconductor and

[1]Department of Physics and Astronomy, Vanderbilt University, Nashville, TN 37235 USA. [2]Vanderbilt Institute of Nanoscale Science and Engineering, Vanderbilt University, Nashville, TN 37235, USA. [3]Department of Chemistry, Vanderbilt Institute of Nanoscale Science and Engineering, Vanderbilt University, Nashville, TN 37235 USA.
*Corresponding author. Email: richard.haglund@vanderbilt.edu

metal plasmons to distinguish it from the directional plasmon-induced resonant energy transfer process, in which the plasmonic dipole of metallic NPs excites an electron-hole pair in a proximate semiconductor (*26*–*28*).

The HIPRET process occurs on the sub-picosecond timescale at excitation energies below the threshold for exciton creation in the semiconductor and serves as the intermediate stage to enhance even high-order harmonic generation (*29*). To characterize the mechanism of HIPRET, we deposit alumina films of varying thickness between Au and CuS NP layers to measure the distance dependence of the harmonic emission. We use finite-difference time-domain (FDTD) simulations in Lumerical to model the near-field enhancement induced by plasmonic interactions in the Au/CuS heterostructure under 1050-nm excitation. The simulated coupling efficiency matches well to the experimental results, both featuring d^{-6} dependence, and strongly implies that the plasmon-plasmon coupling in the Au/CuS heterostructure is mediated by the surface dipoles. Moreover, ultrafast transient absorption (TA) spectroscopy of CuS plasmon dynamics shows that resonant energy transfer between CuS and Au reduces the plasmon relaxation time by about one-third compared to the relaxation time of the CuS plasmon alone. Based on the theory of plasmon-coupled resonant energy transfer (*30*), we established a theoretical framework to elucidate harmonic-induced resonant energy transfer and qualitatively demonstrate the distance dependence of the field-enhancement effect and the harmonic generation signal, as mediated by the plasmonic interaction between Au and CuS NPs. Last, when the pump frequency is substantially detuned from the fundamental plasmon resonance of CuS, the dominant upconversion mechanism is found to change from harmonic generation to MPPL. This observation underscores the critical importance of the harmonic condition between the LSPRs and the pump wavelength on the efficiency of HIPRET—and thus, the total upconversion signal—in the Au/CuS hybrid films.

RESULTS

Distance dependence of harmonic intensity

CuS and Au NPs are synthesized using a chemical solvothermal technique (*31*, *32*). The anisotropic, hexagonal CuS NPs, with average diameter of 18 ± 4 nm and concentration of 2.33×10^{14} particles/ml, oriented face up on the substrate, exhibit a broad plasmon resonance in the near-infrared (NIR) region. Spherical Au NPs, with average diameter of 12 ± 1 nm and concentration of 5.83×10^{14} particles/ml, exhibit a narrow plasmon resonance centered at 525 nm. These NPs are sequentially assembled into heterostructure films by spin coating, and the hybrid films feature two distinct LSPRs originating from Au and CuS, respectively.

In previous work, an oleylamine layer separated the NPs within the films by a few nanometers, thereby preventing direct contact. In the present work, the ligands evaporate during the high-temperature alumina deposition, and the alumina provides a larger, variable separation between NPs. Without this separation, strong electronic charge transfer between the NP layers would quench the LSPRs (*33*). In addition, the interaction among homogeneous NPs is negligible compared to that between NPs in the heterostructured films, as evidenced by the low intensity harmonics generated in homogeneous Au and CuS NP films (*34*, *35*). Previously, we reported that the yields of second-harmonic and cascaded third-harmonic emission in dual-plasmon Au/CuS films were enhanced by factors of 3.3 and 20, respectively, compared to the incoherent sum of the emissions from the individual NPs. However, control over the separation distance between the plasmonic films was limited by length of oleylamine ligands; therefore, the mechanism by which plasmonic interactions contribute to these enhanced nonlinear processes remained ambiguous.

To explore the mechanism underlying the plasmonic interactions, an approach to accurately control the separation between the CuS and Au layers is desirable. The previously employed bath method of NP deposition cannot provide precise control over the amount and length of the coordinating ligands between the Au and CuS NPs; thus, there was no reliable way to adjust separation at the nanometer scale. Attempts to change the separation distance between the NP layers by changing the length of the interlayer ligand failed, likely due to the presence of multiple intercalated layers of ligands instead of a single monolayer.

Here, we develop an alternate approach using a spacer layer of alumina. First, we deposit the Au NPs on the microscope slide by spin coating, and then, we deposit the alumina layer on top of the Au NPs by electron-beam evaporation. The high temperature and vacuum conditions during alumina deposition facilitates the removal of ligands attached to the NPs. Last, we deposit the CuS NPs atop the alumina layer by spin coating (Fig. 1A). We confirm the thicknesses of alumina films (5 nm, 6 nm, 10 nm, 30 nm, 50 nm, 60 nm) using atomic force microscopy (AFM). We characterize the uniformity of the Al_2O_3layer deposition on Au films using energy dispersive spectroscopy (EDS), and the nearly uniform distribution of the Al_2O_3 layers justifies using the thickness of the Al_2O_3 layer to approximate the separation distance between Au and CuS films (figs. S2 A-C). We measure the absorption spectrum of the Au-Al_2O_3-CuS structure using ultraviolet-visible (UV-vis–NIR) spectrophotometry (Fig. 1B). The existence of the Al_2O_3 layers does not shift either LSPR feature in the hybrid structure. In addition, the higher refractive index of alumina improves electric-field confinement around the NPs and narrows the spectral linewidth, thereby increasing the *Q* factor of the plasmon resonance, as shown in Fig. 1B.

To experimentally explore the distance dependence of harmonic generation, we use Al_2O_3 spacer layers of varying thickness. The harmonic generation measurement scheme for the Au/CuS films has been described previously (*34*, *35*). Each Au/CuS bilayer NP film with its defined separation between the Au and CuS layers is exposed to 150-fs pulses from a mode-locked Nd:glass laser operating at 1050 nm. We have demonstrated that the alumina layer does not appreciably reduce the interaction between Au and the pump beam (fig. S4). The plots of the SHG and THG intensities at the peak excitation laser intensity are measured as a function of spacer thickness (Fig. 1, C and D). Both the SHG and THG peak intensities decrease markedly as the separation distance increases from 5 to 10 nm and reveal a sharp inflection for distances larger than 10 nm. Beyond this distance, the SHG and THG intensities show little variation, and the bilayer films produce a relatively low overall harmonic generation signal. We interpret these results to indicate that at separations beyond 10 nm, Au and CuS NPs act independently, and the intense local electric fields from their surface plasmon resonances are effectively shielded from each other by the insulating alumina layers so that the plasmon-plasmon coupling is greatly depressed. At smaller distances, the local electric fields from the surface plasmons spatially overlap and interact. This demonstrated effective distance dependence is consistent with the classic Förster or fluorescence resonant energy transfer (1 to 10 nm) (*36*), suggesting a dipolar resonant energy transfer mechanism.

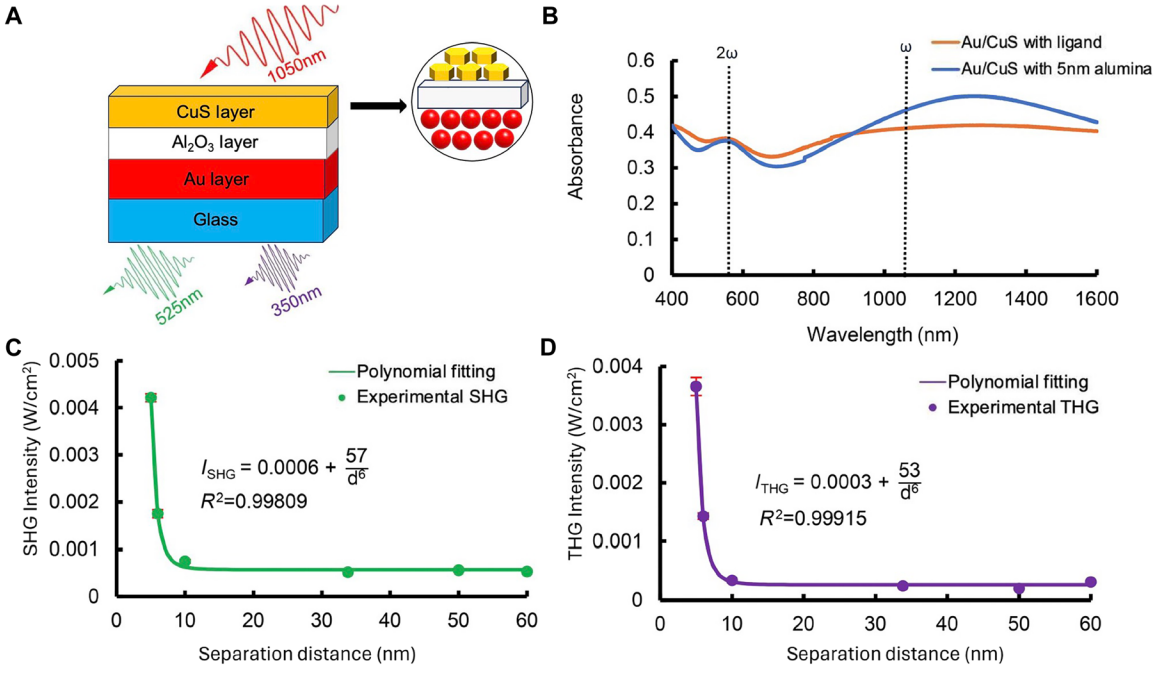

Fig. 1. Separation-distance–dependent SHG and THG in Au/ Al_2O_3/CuS dual-plasmon NP heterostructures. (**A**) Schematic diagram of the Au/Al_2O_3/CuS structure illustrating the second-harmonic and third-harmonic signal generated from 1050-nm pump. (**B**) UV-vis-NIR spectrophotometry of the heterostructure films with different interstitial layers: Au/CuS with 5-nm alumina (blue) and Au/CuS with ligand (orange). The peak harmonic generation intensity with error bars included as a function of the separation distance along with the polynomial fitting function. (**C**) SHG and (**D**) THG at pump intensity of 0.07 GW/cm^2.

We find that the SHG peak intensity versus distance is indeed best fit by the function $I_{SHG} = 0.0006 + \frac{57}{d^6}$, and the THG peak intensity versus distance by $I_{THG} = 0.0003 + \frac{53}{d^6}$. The fitting parameters 0.0006 and 0.0003 W/cm^2 in the functions correspond, respectively, to the incoherent sum of SHG and THG intensities from Au and CuS NPs without plasmonic coupling, consistent with the measurements at large spacer thickness (Fig. 1, C and D), and Eqs. 1 and 2 below. The fitting parameters 57 and 53 GW·nm^6/cm^2 represent the plasmonic coupling strength in the respective plasmon-enhanced harmonic generation, accounting for various coupling factors including the transition dipoles and orientation factors (Supplementary Text) (*30*). The comparable coupling strengths suggest that the plasmonic interactions shape both the SHG and THG output through a similar resonant energy transfer process. The strong agreement [coefficient of determination (R^2)] between experimental results and the fits indicates that a d^{-6} dependence and our theoretical framework is a good approximation of the plasmonic coupling between the Au and CuS NPs.

The dependence of harmonic generation on the distance between the NP layers can be calculated using a model of plasmon coupling dynamics. In Supplementary Text , we develop theoretical expressions for the enhanced THG and SHG mediated by plasmonic interactions. When the CuS and Au NPs are irradiated at high laser intensity, the second-harmonic polarization of the CuS plasmon resonance dipoles and the Au plasmon resonance dipoles are induced via two-photon absorption, contributing to the production of second-harmonic light. These dipolar resonances can couple and transfer second-harmonic energy through nonradiative near-field interactions. This interchange of second-harmonic energy from nearby plasmons can either contribute to the emission of second-harmonic light or combine with a photon from the pump laser to generate third-harmonic light by cascaded THG: $2\omega + \omega = 3\omega$. The SHG and THG intensities from Au/CuS heterostructure films can be expressed as a function of separation distance between the CuS and Au NPs as follows

$$I_{SHG}^{Au/CuS}(2\omega) = \left[I_{pump}^{Au}(2\omega) + I_{pump}^{CuS}(2\omega)\right] + \frac{A_{CuS-Au} + A_{Au-CuS}}{d^6} \quad (1)$$

$$I_{THG}^{Au/CuS}(3\omega) = \left[I_{pump}^{Au}(3\omega) + I_{pump}^{CuS}(3\omega)\right] + \frac{\left(A_{CuS-Au}B_{Au} + A_{Au-CuS}B_{CuS}\right)I(\omega)}{d^6} \quad (2)$$

where $I(\omega)$ is the pump intensity, A_{CuS-Au} (A_{CuS-Au}) is the coefficient of coupling from CuS (Au) to Au (CuS) and B_{Au} (B_{CuS}) is a combined factor relating the efficiency of sum-frequency generation in Au (CuS). In our theoretical model, both $I_{SHG}^{Au/CuS}$ and $I_{THG}^{Au/CuS}$ consist of two terms: The first term is the incoherent sum of harmonic emission from Au and CuS NPs independently, without the coupling effect; the second term represents the enhanced harmonic signal produced by the plasmonic interaction, which displays an inverse-sixth power distance dependence (d^{-6}), consistent with a dipole-dipole interactions. Both the second- and third-harmonic light from the experiments and theory exhibit inverse-sixth power dependence, strongly indicating that the harmonic generation enhancement effect observed in the dual-plasmon heterostructure arises from plasmon-plasmon interactions.

Plasmonic near-field enhancement

We carry out FDTD simulations in Lumerical to further investigate the local electric field enhancement due to coupling of the Au and CuS surface plasmons. To model the harmonic plasmonic resonance,

the polarization of the incident light is set parallel to the basal plane of CuS, in which the NIR in-plane mode of CuS LSPRs dominates (fig. S6A). The simulated extinction spectrum coincides with experimental results, showing distinct LSPRs: a narrow plasmon resonance at 525 nm and a broad plasmon resonance around 1300 nm from the Au and CuS NPs, respectively (fig. S6B). Although the peak positions of the two plasmons are reproduced in the simulated absorption spectrum, we observe a mismatch in the relative amplitudes of the two absorption peaks in our simplified model we use. We simulate the field coupling between a single Au and CuS NP with an average size and idealized shape; however, in the experimental films, the differences in Au and CuS concentrations, differences in lateral concentrations in the spin-coating process, interparticle interactions, and collective coupling between NPs of the same species (Au-Au and CuS-CuS) can modify the relative intensities of the two LSPR peaks. Moreover, NPs in the experimental NP films exhibit a distribution of sizes and shapes, whereas the single-particle simulation assumes uniform average particles. Last, variations in morphology affect the local plasmonic response and can lead to shifted peak intensities, thereby altering the relative amplitudes compared to the idealized model. In our simulation, the CuS is aligned such that its basal plane is parallel to the Au surface, which reproduces the physical orientation (*35*). The two NPs are moved along the diagonal with increasing separation distance, so that the orientation of the CuS edge with respect to the Au plasmon field is unchanged (Fig. 2A). The simulation also shows that an offset along the *y* axis is needed between the Au and CuS to facilitate direct interference of their optical near fields. When the Au and CuS particles are collinear with the excitation direction (fig. S7), the enhanced fields at the vertices of the particles do not overlap, and the near-field distribution demonstrates extremely weak coupling at the smallest separation distances (2 nm), after which there is no field enhancement between the two NPs. When there is an offset between the CuS and Au NPs, there is substantial spatial overlap of the near fields.

Under 1050-nm excitation, we compute the electric field distribution for 2-, 3-, 4-, 6-, 10-, 15-, and 20-nm separation distance—as defined from the edge of the CuS to the nearest surface of the Au sphere (Fig. 2C). As derived in Supplementary Text , the harmonic-induced resonant energy transfer rate is proportional to the square of the near-field strength induced by coupled plasmon resonances

$$W_{\mathrm{HIPRET}}(\omega)=\frac{\eta_n}{\tau_n}\cdot\frac{9c^4}{8\pi}\cdot\left|\frac{\mathbf{E}_{\mathrm{nf}}}{\mu_n}\right|^2\cdot\int d\omega\frac{\epsilon_{\mathrm{Au}}(\omega)F_{\mathrm{CuS}}(\omega)}{(\omega)^4} \quad (3)$$

where n = Au, CuS, respectively, for the bidirectional energy transfer process, η_n is the conversion efficiency of SHG of donor NPs, τ_n is the donor plasmon lifetime, μ_n is the transition dipole, $F_{\mathrm{CuS}}(\omega)$ represents the absorption spectrum of CuS, and $\epsilon_{\mathrm{Au}}(\omega)$ represent the emission spectrum of Au. The representation of harmonic-induced resonant energy transfer presented here is based on the plasmon-coupled resonant energy transfer rate introduced by Schatz (*30*). Thus, the distance dependence of the square of the near-field enhancement (SNFE), directly obtained from the simulation could provide a critical clue to the nature of the plasmon-plasmon coupling. The near-field enhancement is measured at a point 1 nm from the Au surface on the diagonal between the NPs and is fixed for all the separation cases. The measurement position is chosen within the effective

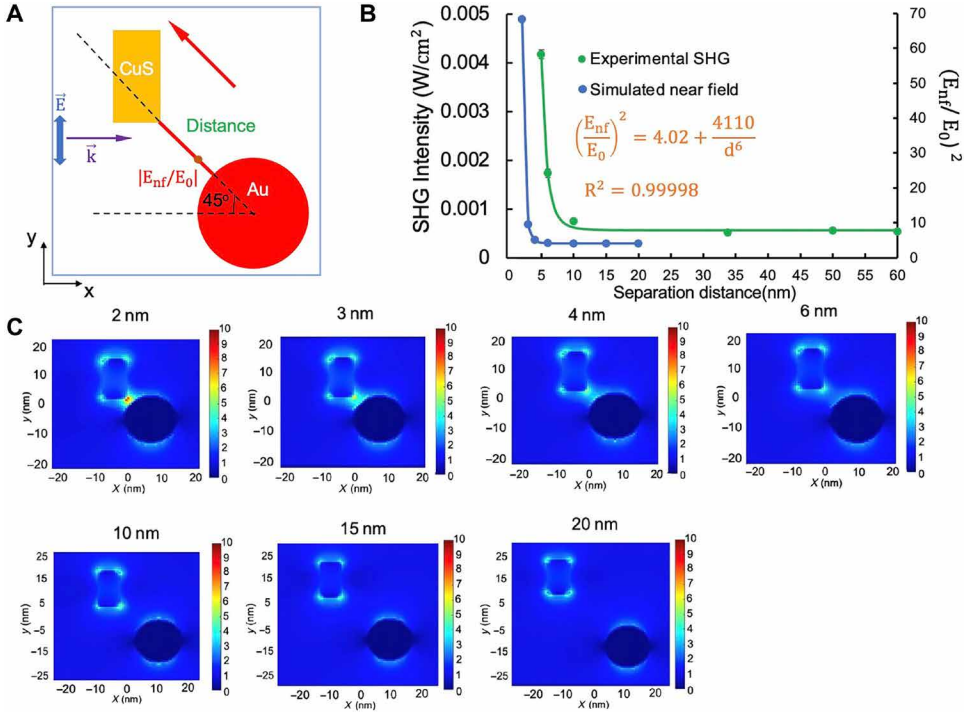

Fig. 2. Near-field coupling simulation between plasmonic Au and CuS NPs. (**A**) Structural model of Au/CuS NPs in the FDTD simulation. The red arrow indicates the direction of NP movement, purple arrow indicates the incident wave-vector, and the blue arrow indicates the electric field polarization. We evaluate the $|E_{nf} / E_0|$ at the orange point. (**B**) Experimental SHG intensity and simulated SNFE as a function of the separation distance with the inverse-sixth power polynomial fit. (**C**) FDTD calculated local electric field distribution with the varying separation distance between the Au and CuS NPs. The color scale bars show the relative increase in the electric field $|E_{nf} / E_0|$.

plasmonic coupling distance (10 nm) closer to the Au, between the Au and CuS NPs, to avoid any influences from hotspots at the corners of the CuS NP (Fig. 2C). The best polynomial fit for the distance-dependent SNFE plot: $\left(\frac{E_{nf}}{E_0}\right)^2 = 4.02 + \frac{4110}{d^6}$ gives an inverse-sixth power distance dependence matching that of the experimental finding for SHG and THG measurements. The fitting parameter 4.02 in the function indicates the Au NPs near-field enhancement effect when the separation distance is sufficiently large that the two NPs function as independent dipoles. When the distance separating CuS and Au NPs is set to larger than 6 nm in the calculation, only weak near-field enhancement is observed.

In addition, we conduct simulations where the separation distance between the Au and CuS is changed by moving the NP along the *x* (fig. S8) and *y* axes independently (fig. S9). The distance dependence of the calculated SNFE also fits an inverse-sixth power distance dependence (fig. S10). The agreement demonstrated in these results regardless of different relative orientation strongly suggests the direct coupling of the surface dipoles between the Au and CuS NPs as a general mechanism for the plasmonic interactions.

In Fig. 2B, we also present a comparison between the experimental and simulated results. Both agree on the distance dependence as stated previously. However, there is a discrepancy between the inflection distances: 6 nm for the simulation and 10 nm for the experiments. The discrepancy can be attributed to the nonuniform deposition of alumina layers on the Au films, as observed in the SEM images (fig. S2, D and E). Although EDS confirms that most of the Au NPs are covered by the deposited alumina layers (fig. S2, B and C), some small Au NPs (the bright spots) remain uncovered by the alumina and are thus directly in contact with CuS. As a result, the effective average distance between the Au and CuS NPs in our structure is smaller than the alumina layer thickness (Fig. 2B). Despite this limitation, the inverse sixth-power distance dependence of plasmon-plasmon coupling efficiency, seen in both experimental far-field harmonic radiation and theoretical near-field enhancement, identifies the plasmonic interaction mechanism as dipole-dipole coupling.

Ultrafast plasmon dynamics

To further investigate the resonant energy transfer between CuS and Au plasmons, we examine the relaxation dynamics in both Au/CuS heterostructure and pure CuS using ultrafast pump-probe measurements (fig. S11). Numerous studies have demonstrated that alumina acts as a passive substrate in the transient region under visible and NIR pump conditions when the plasmonic NPs are nearby (*37*, *38*). The absorption spectrum of Au/CuS includes a broad peak spanning wavelengths from 900 to 2600 nm that corresponds to the CuS plasmon (fig. S15A). The films are pumped at 1200 nm and probed at 2400 nm by synchronized beams from a Light Conversion TOPAS optical parametric amplifier (OPA) with an amplified Ti:sapphire pump to obtain the dynamics of the excited-state absorption (Fig. 3, A and B). While TA changes are observed for both CuS and Au/CuS films, no transient signals in Au NP film absorption are detected because the pump wavelength is not resonant with the Au plasmons, nor do Au NPs strongly absorb the 1200-nm pump light, as seen in the measured absorbance of Au NPs (fig. S15B). The risetime we observe here (~130 fs) is considerably longer than that of the pump pulse (83.2 fs), which indicates a noninstantaneous transient system response. This rise time delay can be attributed to a Kerr-like effect in which the refractive index and absorption coefficient undergo a time-dependent modulation induced by pump-generated hot carriers. When excited by a femtosecond pump pulse, nonequilibrium hot carriers are generated following plasmon decay: These hot carriers excite third-order nonlinearities and drive the temporal response of the NPs (*39*, *40*).

We fit the transient kinetics with a double exponential function and demonstrate strong evidence for plasmonic energy transfer (Table 1). For CuS plasmon dynamics, the rise time can be attributed to hole-hole scattering, while the recovery time can be attributed to hole-phonon scattering (*41*, *42*). The rise time is ~150 fs for all the systems containing CuS. However, the relaxation dynamics reveal a 25% faster decay in the Au/CuS heterostructure (690 fs) than in CuS films (929 fs). The faster Au/CuS relaxation can be attributed to the fact that the HIPRET process between CuS and Au provides an

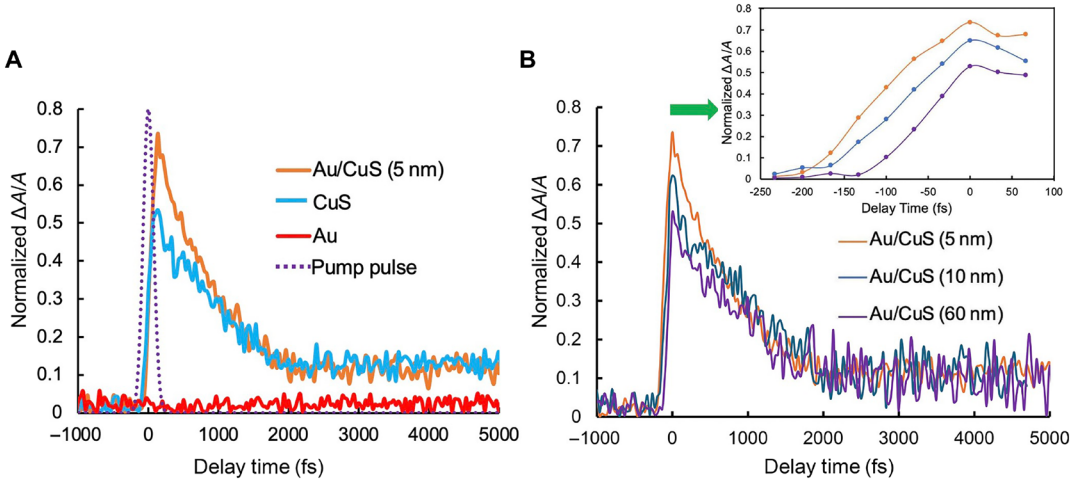

Fig. 3. Ultrafast pump-probe measurement of plasmonic NP heterostructures. Normalized TA dynamics of (**A**) Au/CuS, CuS, and Au. The pump pulse is shown with a dotted dashed line. (**B**) Heterostructure Au/CuS films with different separation distances probed at 2400 nm upon 1200-nm photoexcitation at pump fluence of 1.12 mJ/cm^2. The inset shows the comparison of the rise time.

Table 1. Transient absorption growth and recovery kinetics. Pump: 1200 nm; probe: 2400 nm.

System	τ_{rise}(fs)	$\tau_{recovery}$(fs)
Au/CuS (5 nm)	130±12	690±3
Au/CuS (10 nm)	132±18	937±10
Au/CuS (60 nm)	161±25	955±25
CuS	173±17	929±3

energy-decay pathway in addition to hole-phonon scattering present in pure CuS. We also measure the dynamics in Au/CuS films with different separation distances (Fig. 3B). As the inter-layer spacing grows past the effective coupling distance (10 nm), the relaxation time reverts to that of isolated CuS NPs. This is consistent with our observations in harmonic generation measurements, where there is little SHG and THG enhancement beyond that separation distance (Fig. 1, C and D). In fig. S15A, we compare the absorbance of Au/CuS films with alumina spacer layers of 5-, 10-, and 60-nm thickness. They exhibit nearly identical absorbance at the pump wavelength, indicating that even under the high pump fluence used in our experiments, the longer CuS plasmon recovery time observed in heterostructures with increased spacer thickness arises not from increased electronic heat capacity but from less effective coupling between Au and CuS plasmons (*43*, *44*). Faster plasmon relaxation from our ultrafast studies strongly indicates the presence of HIPRET between CuS and Au plasmons in the heterostructure films. It is worth noting that all Au/CuS and CuS TA signals exhibit a consistent tail with a value of $\Delta A / A \sim 0.1$ at a delay time of 5000 fs. Limited by the maximum delay time in our delay stage, our experiments probe the plasmon decay dynamics via hole-phonon scattering on a timescale of only a few picoseconds. Thereafter, the TA signal is expected to decay as the hot carriers thermalize with the lattice; final relaxation via phonon–phonon scattering takes place over timescales ranging from a few hundred picoseconds to several nanoseconds (*45*, *46*).

Harmonic-induced plasmonic resonant energy transfer

Thus, we can conclude that, in our coupled two-plasmonic system, ultrafast HIPRET between the Au and CuS NPs serves as the mode of action for enhanced SHG and cascaded THG. We perform high intensity absorption measurements on CuS and Au NP films individually (Fig. 4). A decrease in the absorption of CuS under high-intensity 1050-nm excitation indicates saturation of its linear absorption, which means the resonant response of the CuS NPs is maximized. These strong local electric fields contribute to the generation of second-order polarization and thus second-harmonic emission, as in ordinary nonlinear plasmonic enhancement. In contrast, the Au NPs exhibit an increase in absorption as intensity increases. The Au NPs do not have high absorption at 1050 nm at low intensity, and so this increased absorption with pump intensity suggests that two-photon absorption, exciting the fundamental mode of the LSPR at 525 nm, is occurring. However, two-photon absorption is inefficient in CuS due to its band structure — which has an indirect gap of 2.5 eV. So the excited state does not decay by exciton formation followed by recombination (two-photon photoluminescence), a different, competitive process dominates. In this alternative process, the excited CuS and Au dipoles can couple with the characteristic inverse

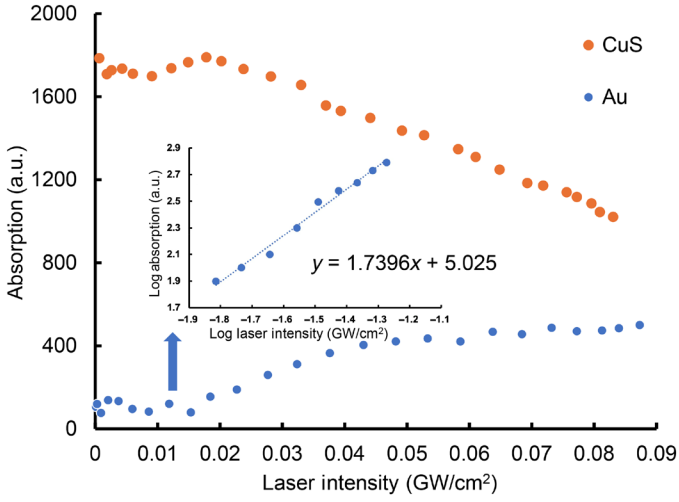

Fig. 4. Nonlinear absorption with high laser intensity. The absorption of CuS and Au films as a function of the input laser intensity at 1050 nm. The inset is the double-logarithmic plots of Au absorption as a function of pump laser intensity above the absorption threshold.

sixth-power distance sensitivity because the spectra of the second harmonic of the CuS plasmon mode and the fundamental plasmon resonance in Au overlap. The energy transferred between the two NPs can then drive the radiation of second-harmonic light or sum-frequency generation with another pump-laser photon to emit at the third harmonic.

Plasmonic couplings for resonant and off-resonant pumping

Thus far, it has been assumed that the harmonic relation of the LSPRs is essential to enhanced harmonic generation via the HIPRET process. While the measured distance dependence is consistent with that model, the hypothesis must be tested by detuning the pump wavelength from the fundamental resonance (1050 nm) in both blue and red directions while collecting the upconverted spectra for comparison to the resonant condition.

For these investigations, we perform an experiment with an Orpheus-F OPA providing excitation wavelengths from 600 to 2000 nm (fig. S16). Experimentally, we blue-shift the pump wavelength to 800 nm and red-shift it to 1200 and 1600 nm and then compare the resulting harmonic yields to those measured under the original experimental condition of 1050 nm (Fig. 5). We observe dominant THG signals at 1050- and 1200-nm pump wavelengths, modest THG at 1600 nm and no measurable THG at 800 nm. In addition, the SHG signal is consistently less intense than the corresponding THG signal at all pump wavelengths, and a peak centered at 717 nm is detected under every excitation condition. The upconverted 717-nm emission is likely from the Au MPPL due to the radiative recombination of the *sp*-band electrons with the *d*-band holes triggered by the sequential steps of the photon absorption, which is consistent with a previous report (*47*).

We plot the THG and SHG intensities as a function of the input laser intensity for different pump wavelengths (Fig. 6, A and B). We observe the highest third-harmonic intensity under 1050-nm pump excitation, which can be attributed to the enhancement from the cascaded process, as the LSPRs of CuS and Au NPs satisfy the fundamental and second-harmonic condition of 1050-nm excitation, respectively. When the pump frequency is red-shifted from the resonance condition

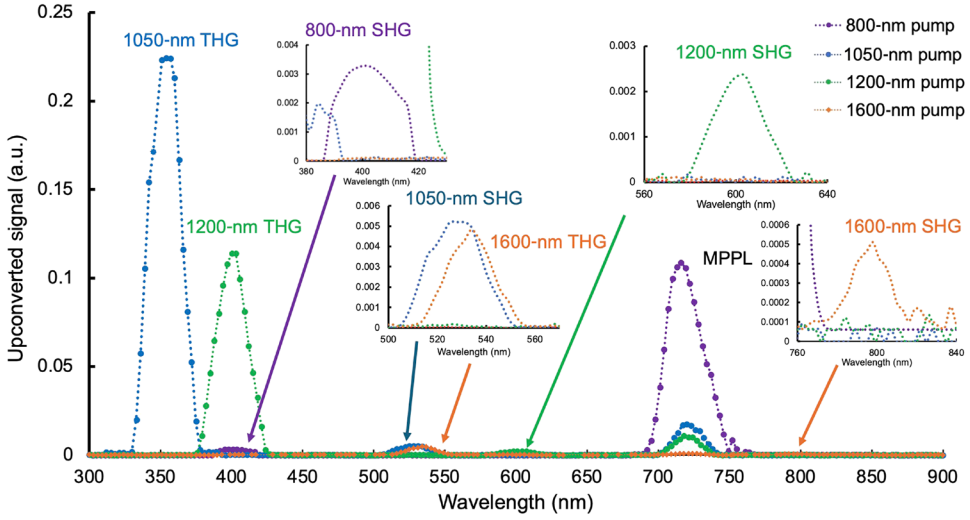

Fig. 5. Pump-wavelength-dependent upconverted spectrum. Upconverted signal produced by the Au/CuS heterostructure films under tunable excitation at 800 nm (purple), 1050 nm (blue), 1200 nm (green), and 1600 nm (orange). Insets are zooming for small values.

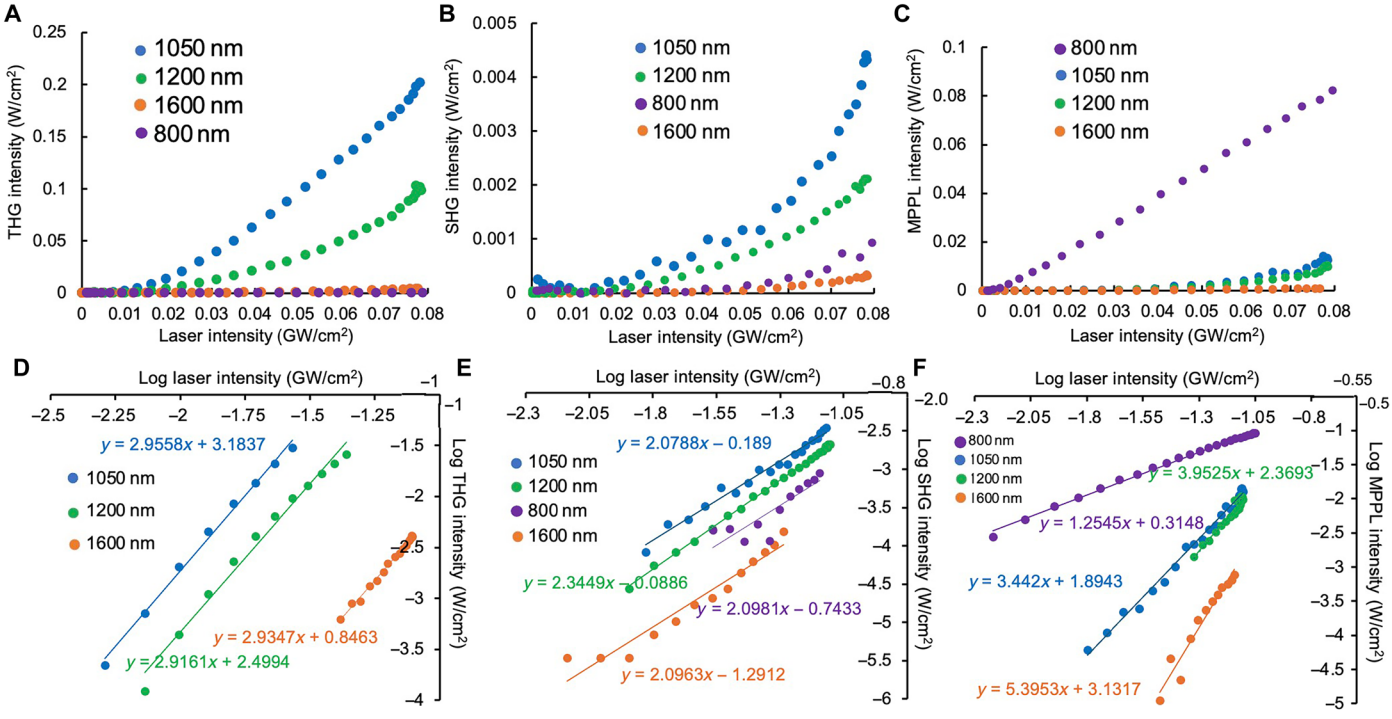

Fig. 6. Upconverted THG, SHG, and MPPL from various pump wavelengths. Intensity of the upconverted signal generated by tunable excitation wavelength as a function of the input laser intensity: (**A**) THG, (**B**) SHG, and (**C**) MPPL. Double-logarithmic plots of output intensity as a function of pump laser intensity: (**D**) THG, (**E**) SHG, and (**F**) MPPL.

at 1050 to 1200 nm, the second harmonic of the 1200-nm pump lies closer to the red edge of the Au LSPR's resonant spectrum, which peaks at 525 nm. Consequently, two-photon excitation of the Au LSPRs occurs less efficiently, and bidirectional HIPRET is reduced (fig. S17), resulting in SHG and THG efficiencies approximately a factor of 2 lower than those achieved with 1050-nm excitation, whose harmonic resonance is centered on the Au plasmon resonance. In contrast to excitation at 1050 and 1200 nm, the SHG and THG from 1600- to 800-nm pump wavelength are much smaller because the fundamental- and second-harmonic frequency of the pump deviates even farther from the peak of the CuS and Au LSPRs, respectively. As a result, the HIPRET process is not triggered at all. The nonlinear orders of the measured harmonic generation signals are confirmed by the log-log plots (Fig. 6, D and E).

The observed photoluminescence signals provide more insight into the upconversion mechanisms with the pump wavelength detuned

from the plasmon resonance (Fig. 6C). An extremely large photoluminescence signal under 800-nm pump excitation stands out. The log-log fitting coefficient is close to 1, which suggests that single-photon photoluminescence in Au dominates the upconversion process in the Au/CuS heterostructure under the 800-nm excitation where the SHG and THG enhancement vanish. The 800-nm pump energy matches the interband transition in Au (*48*) but is not sufficient to trigger excitonic absorption in CuS (2.5 eV, 497 nm) (*49*). The results also show decreasing MPPL intensity as the excitation red-shifts from 800 to 1600 nm. As the pump wavelength increases, the single-photon excitation energy decreases and the number of the photons required for the MPPL process increases, which could be reflected by the increasing slope of the log-log plots (Fig. 6F). Because more photons are required, the electronic transition probability (and MPPL intensity) decreases.

By comparing THG, SHG, and MPPL intensities at various pump wavelengths (Fig. 6 and fig. S19), it can be concluded that the harmonic condition between the plasmon resonances of the NPs and the pump wavelength is essential for the efficient plasmonic interaction and enhanced harmonic generation. As the excitation wavelength is red-shifted from the harmonic condition, the intensities of all the upconverted signals (SHG, THG, and MPPL) are reduced, while blue-shifting the excitation wavelength switches the dominant upconversion process from harmonic generation to MPPL. Our results thus provide direct comparison of resonance and off-resonance plasmon-plasmon coupling on the upconversion mechanism in these multiplasmonic nanostructures.

DISCUSSION

Here, we demonstrate that dual-plasmon Au/CuS heterostructures produce greatly enhanced second-harmonic and cascaded THG via resonant plasmon-plasmon coupling between Au LSPRs and the second harmonic of CuS surface plasmons. By depositing alumina layers of various thicknesses, we precisely manipulate the separation distance between the Au and CuS layers. This separation distance correlates with the inverse sixth-power dependence of harmonic intensities on pump intensity, and experimental measurements are corroborated by FDTD simulation in Lumerical. Transient absorption spectroscopy shows substantially faster plasmon relaxation dynamics in heterostructures than in pure CuS nanocrystals due to transfer of plasmonic energy between CuS and Au NPs. These results demonstrate a bidirectional plasmonic interactions—HIPRET—through which the second-harmonic frequency components generated from the CuS plasmon couples resonantly with the nearby fundamental Au dipolar plasmon modes, resulting in the enhancement of the harmonic emission from both plasmonic counterparts in the heterostructure. Furthermore, we investigate the resonant harmonic condition between the nanoparticulate LSPRs and the pump wavelength. The red-shifted pump wavelength attenuates the upconversion efficiency, while the blue-shifted excitation energy changes the dominant upconversion process from harmonic generation to MPPL.

Our comprehensive study of the fundamental mechanism underlying the plasmon-plasmon interactions in Au/CuS dual-plasmon NP heterostructure illustrates a design strategy for ultrafast, high-efficiency thin-film nonlinear optical nano-devices. The remarkable tunability of the plasmon resonance in these metal-semiconductor nanosystems—achieved by varying the shape, size, composition, and doping level of the semiconductor NPs—enables a broad frequency spectrum for both light absorption and upconversion. In addition, the wide range of possible combinations of the plasmonic metals and semiconductors allows the system to be explored for diverse applications, including spectroscopy, telecommunications, photocatalysis, quantum information, biosensing, and biomedical imaging. One intriguing example is that the high harmonic generation demonstrated in our previous work (*29*) could provide multispectral probes of thin layered materials deposited on top of multiplasmonic layered NP structures (*50*).

The table S1 lists several well-studied plasmonic metal and semiconductor materials along with the wavelengths of their plasmon resonances. These dual-plasmon heterostructures can be investigated for other ultrafast second-order nonlinear processes. For example, by carefully choosing the plasmon resonances of the metal and semiconductor to match the signal (in visible range) and idler (in the NIR range) wavelength of OPA, light at telecom wavelengths (1550 nm) could be efficiently generated by plasmon-enhanced difference frequency generation. Efficient generation of single-photon pairs by spontaneous parametric down-conversion is another possible application, which might lead to quantum information and computation. In metal-semiconductor nanocomposites, by matching the metal and semiconductor LSPRs at the pump and signal frequencies, respectively, pair generation rates are expected to be substantially enhanced.

MATERIALS AND METHODS

Nanoparticle synthesis and film deposition

Nanoparticles of CuS and Au are synthesized using standard solvothermal techniques and then assembled into heterostructure films sequentially by spin coating as described in previous reports (*31*, *32*). The alumina of varying thickness is vertically deposited via electron-beam physical vapor deposition (Angstrom Amod) onto the Au layers after the Au film deposition on the glass slides. The electron beam evaporation is carried out at the pressure $5 \cdot 10^{-6}$ torr, and the electron beam is rastered across the alumina precursor in a crucible while the power increases until the deposition rate stabilizes at 0.3 Å/s, at which point the sample shutter opens and the deposition on the sample initiates. Last, the CuS NPs will be added atop the alumina layers via sputter coating. The thickness of the deposited alumina is verified by AFM (Bruker Dimension Icon AFM) in tapping mode. The structure of the alumina deposition on the Au films is confirmed with scanning electron microscopy (SEM) (Zeiss Merlin SEM) at 1.20 and 10.00 kV with the high-efficiency secondary electron detector and energy dispersive spectroscopy at 10.00 kV and 500 pA (Oxford X-MAX 50 SDD and Oxford Aztec 3.3 EDS analysis software).

Nonlinear optical measurements

The extinction spectrum of the Au-Al_2O_3-CuS films is acquired in the Agilent Technologies Cary 5000 UV-vis–NIR spectrophotometer with an integrating sphere from 400 to 3000 nm. Optical measurements are performed using the nonlinear setup depicted in fig. S16. The Orpheus-F OPA is pumped by a compact, high-repetition rate femtosecond Pharos laser comprising an oscillator and chirped-pulse amplifier, using diode-pumped Yb:KGW [$KGd(WO_4)_2$] as an active medium and generating pulses centered at 1035 ±5 nm at an average power of 600 mW, 187-fs duration, at a repetition rate of 60 kHz, and an energy per pulse of 10 μJ. The signal and idler pulses of the OPA are tunable over 650 to 1000 nm and 1000- to 2500-nm ranges, respectively,

providing gap-free tunability. The laser beam from the OPA is mechanically chopped at a frequency of 265 Hz, with a duty cycle of 20%. This avoids repetitive exposures and ensures stable measurement conditions. To determine the dependence of the upconverted signal on the pump intensity, we use a rotational polarizer to adjust the laser power by varying the angle between the fixed output pump polarization of the pump laser and the axis of the rotational polarizer. Pump power is measured in a Thorlabs S130C power meter with a PM100D readout. The SHG, THG, and MPPL signals are isolated from other upconverted signals using the respective bandpass filter for each pump wavelength (Optosigma VPF-25C-10-25-350 for 1050-nm THG, Optosigma YIF-BA515-560S for 1050-nm SHG and 1600-nm THG, Optosigma VPF-25C-10-12-265 for 800-nm THG, Thorlabs FBH400-10 for 800-nm SHG and 1200-nm THG, Thorlabs FBH600-10 for 1200-nm SHG, and Thorlabs FBH800-10 for 1600-nm SHG). Our detector is the solid-state photomultiplier tube (PMT; Hamamatsu, R9875U for UV light detection and R9880U for visible light detection) operating at 1.1 kV. A Newport ¼ m 74100 Monochromator and the PMT detector are used to collect the output spectrum of the NP heterostructures.

Ultrafast pump-probe measurement

The ultrafast dynamics of NP films are measured using the signal (105 fs, 1200 nm) and idler (130 fs, 2400 nm) beam from a Light Conversion TOPAS OPA pumped by a 1-kHz Ti:sapphire regenerative amplifier (Spectra Physics Spitfire Ace, 100 fs, 800 nm) (*51*). The signal (pump) is chopped at 500 Hz, while the idler (probe) retains a 1-kHz repetition rate. The pump is delayed relative to the probe by computer-controlled delay stage. To ensure probing of a uniformly pumped region, the signal and idler beams are focused to beam waists of 200 and 90 μm, respectively, measured via knife edge experiments. A linear polarizer on a motorized rotational mount adjusts the pump fluence at 1.12 mJ/cm^2. The probe is attenuated using a neutral density filter (ND3) and a linear polarizer to achieve an incident fluence of less than 24 μJ/cm^2. The transmitted probe signal is detected using a PbS-fixed gain detector (Thorlabs PDA30G) via an SR830 lock-in amplifier referenced by the chopper. The transient kinetic traces are plotted with five points movingaverage smoothing. Each curve is normalized to its respective peak differential absorption after subtracting the background signal, defined as the average signal before zero delay. Each normalized differential absorption is calculated using the following equation

$$\text{Normalized}\left(\frac{\Delta A}{A}\right)_i = \frac{\left(\frac{\Delta A}{A}\right)_i - \left(\frac{\Delta A}{A}\right)_{\text{background}}}{\left(\frac{\Delta A}{A}\right)_{\max}} \quad (4)$$

To determine the rate of thermalization due to hole-hole scattering and relaxation due to hole-phonon scattering, the rise time of the TA change is fit to a phenomenological response function (*52*)

$$u(t) = H(t)\left[1-\exp\left(-\frac{t}{\tau_{\text{rise}}}\right)\right]\exp\left(-\frac{t}{\tau_{\text{recovery}}}\right) \quad (5)$$

and the decay trace is fit to the mono-exponential

$$u(t) = A^*\exp\left(-\frac{t}{\tau_{\text{recovery}}}\right) \quad (6)$$

where $H(t)$ is the Heaviside step function and τ_{rise} and τ_{recovery} are the time constants of hole-hole scattering and hole-phonon scattering process.

Optical simulations

The theoretical simulations of the absorption spectra and near-field distributions are performed by commercially available software (Ansys Lumerical FDTD 2021 R2) using a FDTD solver. The material properties of Au sphere (15 nm diameter) are taken from the Johnson and Christy dataset (*53*), while the CuS polygon (base side length of 7.3 nm and 6.7 nm in height) are created as Drude plasma model. The damping constants and plasma frequency of these models are adopted from the reference (*32*). The plane wave centered at 1050 nm is used as the incident pump. The perfectly matched layer boundary conditions are employed in all x, y, and z directions to prevent any nonphysical scattering at boundaries. The grid size in all axes is set to 0.6 nm for the overall simulated region. The simulation time is set to 1000 fs, and the auto shutoff min is set to 10^{-5} s. The absorption cross section is computed by a power monitor, and the near-field patterns in the coupling regions between the Au and CuS NP are examined by a frequency domain field profile monitor.

Supplementary Materials

This PDF file includes:

Supplementary Text
Figs. S1 to S20
Table S1
References

REFERENCES AND NOTES

1. M. Runowski, P. Woźny, I. R. Martín, K. Soler-Carracedo, T. Zheng, H. Hemmerich, F. Rivera-López, J. Moszczyński, P. Kulpiński, S. Feldmann, Multimodal optically nonlinear nanoparticles exhibiting simultaneous higher harmonics generation and upconversion luminescence for anticounterfeiting and 8-bit optical coding. *Adv. Funct. Mater.* **34**, 2307791 (2024).
2. A. D. Francescantonio, A. Zilli, D. Rocco, V. Vinel, L. Coudrat, F. Conti, P. Biagioni, L. Duò, A. Lemaître, C. D. Angelis, G. Leo, M. Finazzi, M. Celebrano, All-optical free-space routing of upconverted light by metasurfaces via nonlinear interferometry. *Nat. Nanotechnol.* **19**, 298–305 (2024).
3. N. Namekata, N. Kobayashi, K. Nomura, T. Sako, N. Takata, S. Inoue, Quantum optical tomography based on time-resolved and mode-selective single-photon detection by femtosecond up-conversion. *Sci. Rep.* **13**, 21080 (2023).
4. R. Czaplicki, J. Mäkitalo, R. Siikanen, H. Husu, J. Lehtolahti, M. Kuittinen, M. Kauranen, Second-harmonic generation from metal nanoparticles: Resonance enhancement versus particle geometry. *Nano Lett.* **15**, 530–534 (2015).
5. T. Shaaran, M. F. Ciappina, R. Guichard, J. A. Pérez-Hernández, L. Roso, M. Arnold, T. Siegel, A. Zaïr, M. Lewenstein, High-order-harmonic generation by enhanced plasmonic near-fields in metal nanoparticles. *Phys. Rev. A* **87**, 3–7 (2013).
6. E. M. Kim, S. S. Elovikov, T. V. Murzina, A. A. Nikulin, O. A. Aktsipetrov, Surface-enhanced optical third-harmonic generation in Ag Island films. *Phys. Rev. Lett.* **95**, 227402 (2005).
7. F. Han, Z. Guan, T. S. Tan, Q. H. Xu, Size-dependent two-photon excitation photoluminescence enhancement in coupled noble-metal nanoparticles. *ACS Appl. Mater. Interfaces* **4**, 4746–4751 (2012).
8. Z. Guan, L. Polavarapu, Q. H. Xu, Enhanced two-photon emission in coupled metal nanoparticles induced by conjugated polymers. *Langmuir* **26**, 18020–18023 (2010).
9. Y. Li, Y. Yang, C. Qin, Y. Song, S. Han, G. Zhang, R. Chen, J. Hu, L. Xiao, S. Jia, Coherent interference fringes of two-photon photoluminescence in individual Au nanoparticles: The critical role of the intermediate state. *Phys. Rev. Lett.* **127**, 73902 (2021).
10. R. A. Farrer, F. L. Butterfield, V. W. Chen, J. T. Fourkas, Highly efficient multiphoton-absorption-induced luminescence from gold nanoparticles. *Nano Lett.* **5**, 1139–1142 (2005).
11. K.-Y. Yang, J. Butet, C. Yan, G. D. Bernasconi, O. J. F. Martin, Enhancement mechanisms of the second harmonic generation from double resonant aluminum nanostructures. *Nano Lett.* **4**, 1522–1530 (2017).

12. M. Ren, S. Liu, B. Wang, B. Chen, J. Li, Z.-L. Li, Giant enhancement of second harmonic generation by engineering double plasmonic resonances at nanoscale. *Opt. Express* **22**, 28653–28661 (2014).
13. G. M. Pan, D. J. Yang, L. Zhou, Z. H. Hao, Q. Q. Wang, Enhanced second harmonic generation by mode matching in gain-assisted double-plasmonic resonance nanostructure. *Sci. Rep.* **7**, 9776 (2017).
14. M. Liu, X. Xue, C. Ghosh, X. Liu, Y. Liu, E. P. Furlani, M. T. Swihart, P. N. Prasad, Room-temperature synthesis of covellite nanoplatelets with broadly tunable localized surface plasmon resonance. *Chem. Mater.* **27**, 2584–2590 (2015).
15. H. Fang, M. Hegde, P. Yin, P. V. Radovanovic, Tuning plasmon resonance of In_2O_3 nanocrystals throughout the mid-infrared region by competition between electron activation and trapping. *Chem. Mater.* **29**, 4970–4979 (2017).
16. X. Ding, C. H. Liow, M. Zhang, R. Huang, C. Li, H. Shen, M. Liu, Y. Zou, N. Gao, Z. Zhang, Y. Li, Q. Wang, S. Li, J. Jiang, Surface plasmon resonance enhanced light absorption and photothermal therapy in the second near-infrared window. *J. Am. Chem. Soc.* **136**, 15684–15693 (2014).
17. Q. Huang, S. Zhang, H. Zhang, Y. Han, H. Liu, F. Ren, Q. Sun, Z. Li, M. Gao, Boosting the radiosensitizing and photothermal performance of $Cu_{2-x}Se$ nanocrystals for synergetic radiophotothermal therapy of orthotopic breast cancer. *ACS Nano* **13**, 1342–1353 (2019).
18. T. Wu, Z. Wang, L. Xiao, P. Qin, Z. Qin, L. Ma, W. Zeng, X. Chen, L. Xiong, G. Fang, Mesoporous Au@$Cu_{2-x}S$ core–shell nanoparticles with double localized surface plasmon resonance and ligand modulation for hole-selective passivation in perovskite solar cells. *Solar. RRL.* **5**, 2100358 (2021).
19. L. Ma, D. Yang, X. Song, H. Li, S. Ding, L. Xiong, P. Qin, X. Chen, Pt decorated (Au nanosphere)/(CuSe ultrathin nanoplate) tangential hybrids for efficient photocatalytic hydrogen generation via dual-plasmon-induced strong VIS–NIR light absorption and interfacial electric field coupling. *Solar. RRL.* **4**, 1900376 (2020).
20. P. Bessel, A. Niebur, D. Kranz, J. Lauth, D. Dorfs, Probing bidirectional plasmon-plasmon coupling-induced hot charge carriers in dual plasmonic Au/CuS nanocrystals. *Small* **19**, 2206379 (2023).
21. M. Sachdeva, N. Ghorai, N. Kharbanda, H. N. Ghosh, Ultrafast plasmonic hot hole transfer and plasmon dynamics in a dual plasmonic Au @ p-$Cu_{2-x}Se$ heterostructure. *Adv. Optical Mater.* **12**, 2301250 (2024).
22. J. M. Yi, D. Wang, F. Schwarz, J. Zhong, A. Chimeh, A. Korte, J. Zhan, P. Schaaf, E. Runge, C. Lienau, Doubly resonant plasmonic hot spot-exciton coupling enhances second harmonic generation from Au/ZnO hybrid porous nanosponges. *ACS. Photonics* **6**, 2779–2787 (2019).
23. C. Li, X. Lu, A. Srivastava, S. D. Storm, R. Gelfand, M. Pelton, M. Sukharev, H. Harutyunyan, Second harmonic generation from a single plasmonic nanorod strongly coupled to a WSe_2 monolayer. *Nano Lett.* **21**, 1599–1605 (2021).
24. J. H. Zhong, J. Vogelsang, J. M. Yi, D. Wang, L. Wittenbecher, S. Mikaelsson, A. Korte, A. Chimeh, C. L. Arnold, P. Schaaf, E. Runge, A. L' Huillier, A. Mikkelsen, C. Lienau, Nonlinear plasmon-exciton coupling enhances sum-frequency generation from a hybrid metal/semiconductor nanostructure. *Nat. Commun.* **11**, 1464 (2020).
25. S. Saini, G. Srinivas, B. Bagchi, Distance and orientation dependence of excitation energy transfer: From molecular systems to metal nanoparticles. *J. Phys. Chem. B* **113**, 1817–1832 (2009).
26. Z. He, F. Li, P. Zuo, H. Tian, Principles and applications of resonance energy transfer involving noble metallic nanoparticles. *Materials* **16**, 3083 (2023).
27. X. C. Ma, Y. Dai, L. Yu, B. B. Huang, Energy transfer in plasmonic photocatalytic composites. *Light. Sci. Appl.* **5**, 16017 (2016).
28. J. Li, S. K. Cushing, F. Meng, T. R. Senty, A. D. Bristow, N. Wu, Plasmon-induced resonance energy transfer for solar energy conversion. *Nat. Photon.* **9**, 601–607 (2015).
29. Y. Yan, N. J. Spear, Q. Meng, M. R. Singh, J. E. Macdonald, R. F. Haglund, Harmonic generation up to fifth order from Al/Au/CuS nanoparticle films. *Nano Lett.* **24**, 5085–5092 (2024).
30. L.-Y. Hsu, W. Ding, G. C. Schatz, Plasmon-coupled resonance energy transfer. *J. Phys. Chem. Lett.* **8**, 2357–2367 (2017).
31. N. R. Jana, L. Gearheart, C. J. Murphy, Seeding growth for size control of 5-40 nm diameter gold nanoparticles. *Langmuir* **17**, 6782–6786 (2001).
32. Y. Xie, L. Carbone, C. Nobile, V. Grillo, S. D'Agostino, F. D. Sala, C. Giannini, D. Altamura, C. Oelsner, C. Kryschi, P. D. Cozzoli, Metallic-like stoichiometric copper sulfide nanocrystals: Phase- and shape-selective synthesis, near-infrared surface plasmon resonance properties, and their modeling. *ACS Nano* **7**, 7352–7369 (2013).
33. R. Estebanm, A. G. Borisov, P. Nordlander, J. Aizpurua, Bridging quantum and classical plasmonics with a quantum-corrected model. *Nat. Commun.* **3**, 825 (2012).
34. N. J. Spear, K. A. Hallman, E. A. Hernández-Pagán, R. B. Davidson, S. L. Arrowood, A. L. Wistuba, W. Tan, R. F. Haglund, J. E. Macdonald, Enhanced broadband and harmonic upconversion from coupled semiconductor and metal nanoparticle films. *ACS Appl. Nano Mater.* **3**, 3144–3150 (2020).
35. N. J. Spear, Y. Yan, J. M. Queen, M. R. Singh, J. E. Macdonald, R. F. Haglund, Surface plasmon mediated harmonically resonant effects on third harmonic generation from Au and CuS nanoparticle films. *Nanophotonics* **12**, 273–284 (2023).
36. P. C. Ray, Z. Fan, R. A. Crouch, S. S. Sinha, Z. Fan, Nanoscopic optical rulers beyond the FRET distance limit: Fundamentals and applications. *Chem. Soc. Rev.* **43**, 6370–6404 (2014).
37. B. Ostovar, S. A. Lee, A. Mehmood, K. Farrell, E. K. Searles, B. Bourgeois, W. Chiang, A. Misiura, N. Gross, A. Al-Zubeidi, J. A. Dionne, C. F. Landes, M. Zanni, B. G. Levine, S. Link, The role of the plasmon in interfacial charge transfer. *Sci. Adv.* **10**, 3353 (2024).
38. K. G. Stamplecoskie, J. S. Manser, Facile SILAR approach to air-stable naked silver and gold nanoparticles supported by alumina. *ACS Appl. Mater. Interfaces* **6**, 17489–17495 (2014).
39. H. Baida, D. Mongin, D. Christofilos, G. Bachelier, A. Crut, P. Maioli, N. D. Fatti, F. Vallée, Ultrafast nonlinear optical response of a single gold nanorod near its surface plasmon resonance. *Phys. Rev. Lett.* **107**, 057402 (2011).
40. M. Maiuri, A. Schirato, G. Cerullo, G. D. Valle, Ultrafast all-optical metasurfaces: Challenges and new frontiers. *ACS Photonics* **11**, 2888–2905 (2024).
41. J. Zhu, J. Dai, Y. Xu, X. Liu, Z. Wang, H. Liu, G. Li, Photo-enhanced dehydrogenation of formic acid on Pd-based hybrid plasmonic nanostructures. *Nanoscale Adv.* **5**, 6819–6829 (2023).
42. A. M. Brown, R. Sundararaman, P. Narang, W. A. Goddard III, H. A. Atwater, Nonradiative plasmon decay and hot carrier dynamics: Effects of phonons, surfaces, and geometry. *ACS Nano* **10**, 957–966 (2016).
43. C. Voisin, N. D. Fatti, D. Christofilos, F. Vallée, Ultrafast electron dynamics and optical nonlinearities in metal nanoparticles. *J. Phys. Chem. B* **12**, 2264–2280 (2001).
44. N. D. Fatti, F. Vallée, C. Flytzanis, Y. Hamanaka, A. Nakamura, Electron dynamics and surface plasmon resonance nonlinearities in metal nanoparticles. *Chem. Phys.* **251**, 215–226 (2000).
45. J. G. Liu, H. Zhang, S. Link, P. Nordlander, Relaxation of plasmon-induced hot carriers. *ACS. Photonics* **5**, 2584–2595 (2018).
46. M. Perner, P. Bost, U. Lemmer, G. V. Plessen, J. Feldmann, U. Becker, M. Menning, M. Schmitt, H. Schmidt, Optically induced damping of the surface plasmon resonance in gold colloids. *Phys. Rev. Lett.* **78**, 2192–2195 (1997).
47. V. Knittel, M. P. Fischer, T. D. Roo, S. Mecking, A. Leitenstorfer, D. Brida, Nonlinear photoluminescence spectrum of single gold nanostructures. *ACS Nano* **9**, 894–900 (2015).
48. Z. Ebrahimpour, N. Mansour, Plasmonic near-field effect on visible and near-infrared emissions from self-assembled gold nanoparticle films. *Plasmonics* **13**, 1335–1342 (2018).
49. S. K. Nath, P. K. Kalita, Effect of growth condition on the structural, optical and ionic characteristics of chemically synthesized CuS nanostructures in starch matrix. *Bulg. J. Phys.* **50**, 280–300 (2023).
50. C. Heide, Y. Kobayashi, S. R. U. Haque, S. Ghimire, Ultrafast high-harmonic spectroscopy of solids. *Nat. Phys.* **20**, 1546–1557 (2024).
51. K. A. Hallman, K. J. Miller, A. Baydin, S. M. Weiss, R. F. Haglund, Sub-picosecond response time of a hybrid VO_2: Silicon waveguide at 1550 nm. *Adv. Optical. Mater.* **9**, 2001721 (2021).
52. C. Voisin, D. Christofilos, N. D. Fatti, F. Vallée, Size-dependent electron-electron interactions in metal nanoparticles. *Phys. Rev. Lett.* **85**, 2200–2203 (2000).
53. P. B. Johnson, R. W. Christy, Optical constant of the noble metals. *Phys. Rev. B.* **6**, 4370–4379 (1972).
54. R. W. Boyd, *Nonlinear Optics Fourth Edition* (Academic Press, 2020), chap 2.

Acknowledgments

Funding: Y.Y. and A.J.C. are thankful to the Vanderbilt Department of Physics and Astronomy for graduate assistantships. R.F.H. acknowledges the funding from the Stevenson Endowment in Vanderbilt Physics Department. **Author contributions:** Conceptualization: Y.Y., N.J.S., J.E.M., and R.F.H. Investigation: Y.Y., N.J.S., A.J.C., and R.F.H. Methodology: Y.Y., A.J.C., J.E.M., and R.F.H. Resources: Y.Y., A.J.C., J.E.M., and R.F.H. Data curation: Y.Y. and A.J.C. Formal analysis: Y.Y., A.J.C., and R.F.H. Validation: Y.Y., N.J.S., A.J.C., K.K., and R.F.H. Software: Y.Y. and A.J.C. Visualization: Y.Y., K.K., and R.F.H. Writing—original draft: Y.Y. Writing—review and editing: Y.Y., N.J.S., A.J.C., K.K., J.E.M., and R.F.H. Supervision: J.E.M. and R.F.H. Funding acquisition: J.E.M. and R.F.H. Project administration: R.F.H. Y.Y., N.J.S., A.J.C., K.K., J.E.M., and R.F.H. have given approval to the final version of the manuscript. **Competing interests:** The authors declare that they have no competing interests. **Data and materials availability:** All data needed to evaluate the conclusions in the paper are present in the paper and the Supplementary Materials.

Submitted 9 December 2024
Accepted 29 April 2025
Published 4 June 2025
10.1126/sciadv.adv1822